

Formal Verification of Local Robustness of a Classification Algorithm for a Spatial Use Case*

Delphine Longuet Amira Elouazzani

Thales, TRT, cortAix Labs
France

name.surname@thalesgroup.com

Alejandro Penacho Riveiros Nicola Bastianello

KTH Royal Institute of Technology
Stockholm, Sweden
{alejpr|nicolba}@kth.se

Failures in satellite components are costly and challenging to address, often requiring significant human and material resources. Embedding a hybrid AI-based system for fault detection directly in the satellite can greatly reduce this burden by allowing earlier detection. However, such systems must operate with extremely high reliability. To ensure this level of dependability, we employ the formal verification tool Marabou to verify the local robustness of the neural network models used in the AI-based algorithm. This tool allows us to quantify how much a model’s input can be perturbed before its output behavior becomes unstable, thereby improving trustworthiness with respect to its performance under uncertainty.

The number of satellites orbiting Earth and their importance have significantly increased in recent decades [7]. Indeed, they serve as the infrastructure for fundamental technologies such as positioning and communication, and enable scientific advancements in Earth observation. However, these satellites are deployed in a difficult environment, which might lead to failures, and are in practice inaccessible for maintenance. Therefore, there is a need to ensure these satellites function without failures throughout their mission. Among the components prone to failure are the Reaction Wheel Assemblies (RWAs), which consist of an electric motor rotating a disk that imparts momentum to the satellite to change its attitude [8]. Thus RWAs have mechanical components in constant motion, making them prone to failures. Given the cost of a failure (potentially terminating a mission), it is important to detect and alert the ground station of possible impending failures.

In this paper thus we focus on a hybrid approach, combining data-driven technique and physics-based insights, to detect anomalies in RWAs that might indicate a future failure. In particular, we focus on detecting four types of anomalies, related to different components of the RWA, each of which has three urgency levels. The full hybrid algorithm is described in [9, 10]. Given the importance of preventing failures in RWAs, the anomaly detection and classification algorithm should be reliable, avoiding false negatives especially, but also false positives to avoid burdening the ground station personnel. Additionally, it should be robust to perturbations in the data, due to *e.g.* unforeseen operating conditions or degradation of the components. Therefore, in this paper we focus on guaranteeing the local robustness of the hybrid algorithm through formal verification, targeting in particular the neural networks that are part of the classification algorithm.

An AI classification model is said to be locally robust¹ for a given perturbation (noise) of the inputs if

*This work was supported by the EU Horizon Research and Innovation Actions program under Grant 101070162.

¹Local robustness is also called stability, for example in the new ML standard ED-324/ARP6983 (ongoing work from the joint EUROCAE/SAE working groups WG-114/G-34).

for any input x classified as y , all the inputs resulting from this perturbation applied to x are also classified as y . It means that the model does not change the classification for an input if it is only slightly modified. Several formal verification tools emerged these last years that aim to provide mathematical guarantees to AI algorithms, aimed in particular at neural networks [12, 5, 2, 13]. These tools take as input a trained neural network N seen as a function $f : I \rightarrow O$ between a set of inputs I and a set of outputs O , and an input-output relationship property of the form $\forall x \in I, (P(x) \wedge f(x) = y) \Rightarrow Q(y)$, where P and Q are predicates for pre- and post-conditions. Based on these inputs, the tools use SMT-based (Satisfiability Modulo Theories) and abstract interpretation techniques to prove the property or find a counter-example.

The classification algorithm developed for the detection of RWAs anomalies implements a hybrid approach where neural networks are used after an analytical data processing phase. Unfortunately, this algorithm was not designed in order to be formally verified, therefore applying formal verification to the whole algorithm is not currently possible. Instead, we propose a methodology that relies on formal methods to increase confidence in its local robustness, establishing local robustness of the neural networks that are part of the classification algorithm by using the tool Marabou based on SMT constraint-solving.

This paper is structured as follows. In Section 1, we discuss the design of the hybrid algorithm [9, 10], which combines data-driven tools and physics-based insights to detect and classify anomalies in satellites' RWAs. We summarize its structure and showcase some illustrative results in terms of classification accuracy. We highlight its resilience on neural network components, motivating the need for a robustness analysis. Section 2 proposes a methodology to achieve local robustness verification of this classification algorithm, using formal verification of the neural networks involved. We explain how this methodology improves confidence even though formal verification of the whole algorithm is not tractable. Results are presented in Section 3. In Section 4, we discuss how we go beyond local robustness by defining sets of inputs for which the classification is certain, thus improving confidence in the global robustness of the algorithm on some particular classes.

1 Algorithm Description

In this section we briefly discuss the proposed anomaly classification algorithm, summarizing its design and showcasing its classification performance. The complete details can be found in [9, 10].

1.1 Problem formulation

We start by formally stating the problem we aim to solve. The goal is to use on-board measurements to classify the status of the RWA, which can be: nominal, or anomaly A, B, C, D, each of which has 3 urgency levels. A higher urgency level corresponds to a higher likelihood that the RWA will break down in the near future, and thus the ground station needs to be notified more quickly of the RWA's anomalous behavior. The data available for the classification are measurements of the spin rate ω_k [rad/s] indexed by $k \in \mathbb{N}$, and measurements of the total friction torque f_k [mNm]. One datapoint is then characterized as the sequence of measurements $\{(\omega_k, f_k)\}_{k=1}^N$, $N \in \mathbb{N}$. Figure 1 depicts an example of the spin rate and friction torque time series. We remark that the friction torque is not directly measured, but rather estimated from the total output torque of the motor.

Problem: using spin rate and friction torque data, classify the status of the RWA as either nominal or anomalous, and in the latter case classify the type of anomaly (A, B, C, D) and its urgency level (1–3).

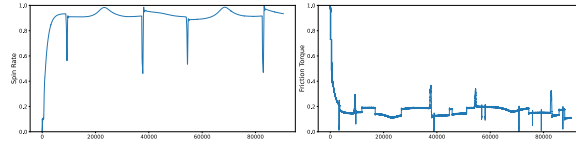


Figure 1: Time series of a RWA spin rate and friction torque

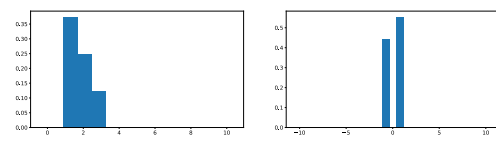


Figure 2: Histograms used to classify anomalies C and D

1.2 Hybrid algorithm design

In this section we summarize the design of the hybrid classification algorithm, which combines data-driven techniques with physics-based insights. We start by discussing the physical foundation of the algorithm.

1.2.1 Physics model

The RWA is a rotating machine, and thus is a friction system characterized by a relationship between spin rate and the friction torque. In our design, we choose to employ the following simple model of this relationship [1]:

$$f_k = f_k^d \text{sign}(\omega_k) + f^v \omega_k + v_k \quad (1)$$

where:

- $f_k^d \text{sign}(\omega_k)$ is the dry friction torque, with magnitude (f_k^d) independent of the spin rate and always opposing the motion of the wheel. f_k^d is indexed by k as it can change over time. Dry friction is caused by the contact between solid surfaces inside the bearings [6]. Anomalies A, C, D affect f_k^d .
- $f^v \omega_k$ is the viscous friction torque, proportional to the spin rate of the wheel and with constant coefficient f^v . This component is due to the lubricant present in the bearings of the RWA [4]. We remark that, although the viscous friction coefficient can be affected by temperature and pressure [11], these changes take place on a longer time scale than the anomalous phenomena we seek to classify in this paper. Anomaly B affects f^v .
- v_k is the noise in the system, which we assume to be normal with zero mean and variance σ , as motivated by e.g. [3].

We remark that this model is not a precise representation of the RWA behavior, which is significantly more complex. Nonetheless, this model serves as a good foundation for the design of the classification algorithm when combined with labeled data.

We turn now to describing the overall classification algorithm. The algorithm is composed of two parts: 1) data processing (see section 1.2.2) and 2) classification based on the processed data (see section 1.2.3).

1.2.2 Data processing

The role of the data processing step is to extract, from the measurements $\{(\omega_k, f_k)\}_{k=1}^N$, the information necessary to classify the anomalies. In particular, the data processing consists of the following steps, depicted also in Figure 3:

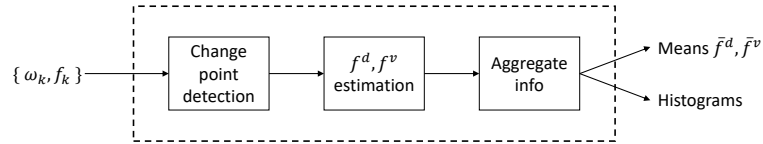


Figure 3: Data processing pipeline.

1. Friction coefficient estimation: the classification step requires the estimation of the values f_k^d and f_k^v from the sequence of measurements f_k . Since model (1) is linear, this can be easily done using linear regression. However, f_k^d undergoes instantaneous changes (both with nominal and anomalous status), and thus is better modeled as a piece-wise constant sequence of values. Thus the following step is required before the coefficients can be estimated.
2. Changepoint detection: since f_k^d is a piece-wise constant sequence of values, the idea is to break down the sequence of measurements in the intervals when f_k^d is constant. To this end, we need to detect when a change in its values occurs. This is performed by fitting the linear model (1) against the sequence of measurements on a rolling window of size much smaller than N . When the linear fit loses accuracy, it means that a change has occurred, and we can divide the sequence in two intervals where f_k^d has two different values. We continue this operation for the whole sequence, ending up with a set of intervals, to which we can individually apply friction coefficient estimation described in 1. We denote by \hat{f}_i^d and \hat{f}_i^v the estimated friction coefficients over the i -th interval.
3. Coefficients estimates processing: after running steps 1. and 2., we have a set of intervals $[k_i, k_{i+1})$, $k_i \in \{1, \dots, N\}$, $k_i < k_{i+1}$, indexed by $i \in \{1, \dots, I\}$, and to each interval we associate the coefficients estimates \hat{f}_i^d and \hat{f}_i^v . The last step then is to process the coefficients estimates to extract the information required for classification of the different anomalies. In particular, we extract the following:
 - (a) The mean values of dry and viscous friction coefficients $\bar{f}^d = \frac{1}{I} \sum_i \hat{f}_i^d$ and $\bar{f}^v = \frac{1}{I} \sum_i \hat{f}_i^v$ – these are used to classify anomalies A and B.
 - (b) The specific distribution of the values \hat{f}_i^d acts as a signature of the anomalies C and D. Therefore, we approximate the two anomalies' distributions via two histograms of the variations in friction coefficient, *i.e.* $\hat{f}_{i+1}^d - \hat{f}_i^d$. In particular, the histogram for anomaly D collects the values of $\hat{f}_{i+1}^d - \hat{f}_i^d$ in M bins, computing their relative frequency to build the histogram. On the other hand, anomaly C is characterized by an increase and subsequent decrease of roughly equal magnitude – that is, $\hat{f}_{i+1}^d - \hat{f}_i^d \simeq -(\hat{f}_{i+2}^d - \hat{f}_{i+1}^d)$. The histogram thus only needs to include information on the first variation in friction torque (the increase), and the M bins collect only these values and their frequency. The construction of these histograms then proceeds as follows: we check for matching pairs of friction torque increase and decrease, and collect the magnitude of the increases in the anomaly C bin, discarding the decreases. The anomaly D histogram is then constructed with the magnitudes of the variations not accounted for before. Figure 2 shows examples of anomaly C and D histograms.

1.2.3 Classification

With the results of the data processing in place, we can now provide an overview of the classification algorithm. The algorithm is structured similarly to a decision tree, where different nodes classify different types of anomalies or whether the status is nominal, see Figure 4. The four classification modules are

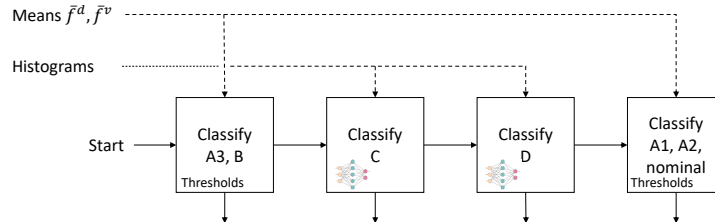


Figure 4: Classification algorithm overview.

designed as follows:

- Classification of A3, B: the classification of anomalies A, B and of nominal behavior can be done via the mean values \bar{f}^d and \bar{f}^v . Indeed, anomaly A corresponds to an increase in \bar{f}^d as compared to the nominal baseline, while anomaly B corresponds to an increase in \bar{f}^v . Additionally, the magnitude of this increase defines the urgency level of the anomaly. The first module then applies threshold checking to discriminate between A3 and B (B1, B2, B3). At this stage we do not classify A1, A2 and nominal, as this might lead to misclassification of anomalies C, D.
- Classification of C, D: the second and third modules then employ the histograms (approximating the distribution of the changes in f_k^d) to classify C and D, and assign an urgency level as well. This classification is performed employing two small-scale neural networks, characterized by 1 hidden layer of 10 neurons, with ReLU activation.
- Classification of A1, A2, nominal: finally, sequences that have not been classified by any of the previous modules are classified based on the values of \bar{f}^d and \bar{f}^v , again using threshold checking.

The overall structure of the algorithm then is designed to minimize misclassification between the types of anomalies. The thresholds and neural networks are trained using examples of $\{(\omega_k, f_k)\}_{k=1}^N$ labeled with an anomaly (or nominal) status, and with an urgency level. For training, we use 40% of the available labeled data, which includes 2000 nominal, 683 anomaly A, 871 B, 792 C, 875 D, each divided equally by urgency level.

1.3 Classification results

In this section we briefly report the results on the accuracy of the classification algorithm applied to a validation set of data. We start by presenting the confusion matrix of the classifier in Table 1, where the columns correspond to the true status and the rows correspond to status output by the algorithms. As we can see, the classification accuracy is generally high when discriminating between different anomalies and nominal. However, there is some misclassifications between nominal and low urgency A, and some misclassifications between different urgency levels of the same anomaly.

We present now the results in terms of additional performance indicators. To define them, we denote by $N(X)$ the total number of datapoints with status X (A-D or nominal), $N_c(X)$ as the number of datapoints with status X correctly classified as X, and $N_{\text{all}}(X)$ as the number of all datapoints classified as status X. Then we define sensitivity as $S(X) = N_c(X)/N(X)$ and positive predictive value as $PPV(X) = N_c(X)/N_{\text{all}}(X)$. Table 2 collects the resulting sensitivity and PPV for the overall classification, and divided by urgency level, and anomaly status. As we can see, these values are very high, exceeding 90% in all but one case.

D3	0.2										19.2	85.6	
D2	0.2									4.4	79.7	14.4	
D1	0.6		1.3							95.6	1.1		
C3								2	100				
C2								98					
C1							100						
B3						100							
B2					99.4								
B1				99.4	0.6								
A3				99.4									
A2		1.1	95.6	0.6									
A1	0.9	92.1	3.1										
N	98.1	6.7		0.6									
	N	A1	A2	A3	B1	B2	B3	C1	C2	C3	D1	D2	D3

Table 1: Confusion matrix between actual status (columns) and status classified by the algorithm (rows). ‘N’ stands for nominal, and an empty cell implies no confusion.

Metric	Result [%]	Metric	Result [%]
S(A+B+C+D)	99.6	PPV(A+B+C+D)	97.1
S(A1+B1+C1+D1)	97.4	PPV(A1+B1+C1+D1)	86.6
S(A2+B2+C2+D2)	92.8	PPV(A2+B2+C2+D2)	90.9
S(A3+B3+C3+D3)	96.3	PPV(A3+B3+C3+D3)	94.8
S(A)	98.0	PPV(A)	98.0
S(B)	99.8	PPV(B)	100
S(C)	100	PPV(C)	100
S(D)	100	PPV(D)	97.4

Table 2: Sensitivity and positive predictive values for different sub-sets of anomalies.

2 Formal Verification Methodology for Local Robustness

Our goal is now to formally prove the local robustness (also called stability) of this classification algorithm. We based our work on a formal verification tool for neural networks called Marabou [13]. Marabou is based on SMT (Satisfiability Modulo Theories) verification techniques and can check arbitrary linear properties over neural networks. Its result is either a formal guarantee that the network satisfies the property, a concrete input for which the property is violated (a counterexample), or inconclusive. In our case, on small-sized neural networks with only ReLU activation functions, Marabou can achieve a complete resolution, therefore the result is always conclusive. It supports feed-forward neural networks with many different linear, piecewise-linear, and non-linear activation functions. Properties can be specified using a Python interface or in a language dedicated to the verification of neural networks called VNN-LIB.² These specifications are expressed as input-output relationship properties. In

²<https://www.vnnlib.org/>

our case, properties are expressed with constraints on the inputs as intervals around each data point, and constraints on the output which ensure that the score for a targeted class remains greater than that of any other class. For a neural network $f : \mathbb{R}^N \rightarrow \mathbb{R}^M$, we define the classification function $Class : \mathbb{R}^N \rightarrow \llbracket 1, M \rrbracket$ as $Class(x) := \arg \max_{i \in \llbracket 1, M \rrbracket} f(x)_i$. Given two vectors $a, b \in \mathbb{R}^N$, and a targeted class $target \in \llbracket 1, M \rrbracket$ a typical property would be:

$$\forall x \in \mathbb{R}^N, (\forall i \in \llbracket 1, N \rrbracket, a_i \leq x_i \leq b_i) \Rightarrow Class(x) = target \quad (2)$$

As described in previous section, the classification algorithm is composed of two phases: a data processing phase, followed by a classification phase using thresholds and neural networks. The output of the data processing phase is composed of several elements, among which are two histograms, used to classify anomalies C and D, using two different neural networks. Our formal verification will focus on proving the local robustness of these two neural networks.

2.1 Problem formalization

For a given dataset input $s = \{(\omega_k, f_k)\}_{k=1}^N \in (\mathbb{R}^2)^N$, the data processing phase of the algorithm returns two histograms $h^C, h^D \in \mathbb{R}^M$, where $M \in \mathbb{N}$, that are used to classify anomalies C and D, respectively³.

We denote by $DP : (\mathbb{R}^2)^N \rightarrow (\mathbb{R}^M)^2$ the data processing function, such that $DP(s) = (h^C, h^D)$. Each histogram is then passed to a neural network³ $NN^C, NN^D : \mathbb{R}^M \rightarrow \llbracket 0, 3 \rrbracket$, which assigns a class label corresponding to four levels: the absence of the anomaly (label 0), or its presence at one of three urgency levels (labels 1 to 3). Following the notations from previous sections, we denote these classes by $\{\text{no C, C1, C2, C3}\}$ and $\{\text{no D, D1, D2, D3}\}$, where label 0 indicates no anomaly.

The complete classification algorithms for anomalies C and D, as defined in the previous paragraph, are denoted by³ $Class^C, Class^D : (\mathbb{R}^2)^N \rightarrow \llbracket 0, 3 \rrbracket$, and are defined as compositions of DP with the respective networks: $Class^C = NN^C \circ DP$ and $Class^D = NN^D \circ DP$.

We denote by $P_\varepsilon^t(s)$ the set of inputs resulting from a chosen perturbation t applied to an input s with strength $\varepsilon \in \mathbb{R}^+$. The local robustness property can then be formulated as follows: the classification algorithm is locally robust for a time series s under perturbation t with strength ε if and only if

$$\forall x \in (\mathbb{R}^2)^N, x \in P_\varepsilon^t(s) \Rightarrow Class(x) = Class(s).$$

In the following, we focus on a single neural network, as the same methodology is applied independently to both classifiers of anomaly C and D.

2.2 Perturbations

For classical perturbations modeled by an L_∞ norm, for instance when inputs are images, we have $P_\varepsilon^t(s) = \{x \mid \|s - x\|_\infty \leq \varepsilon\}$. In our case, we need to consider perturbations relevant to time series. Our discussions with domain experts led to the choice of the following perturbations: random noises (Gaussian, uniform, and Poisson), linear trend perturbation, missing data, and amplitude scaling.

- Random perturbations add to the original signal a noise, which is sampled from the chosen distribution then scaled by parameter ε with respect to the signal amplitude (meaning that if $\varepsilon = 0.01$, the noise is scaled up to 1% of the spin rate, resp. friction, amplitude). We chose Gaussian distribution with mean 0 and variance 1 (see Fig 5b), uniform distribution with values between -1 and 1 (see Fig 5c), and Poisson distribution with parameter 1.

³We will simplify the notations C and D to C when the anomaly type is clear from context or irrelevant.

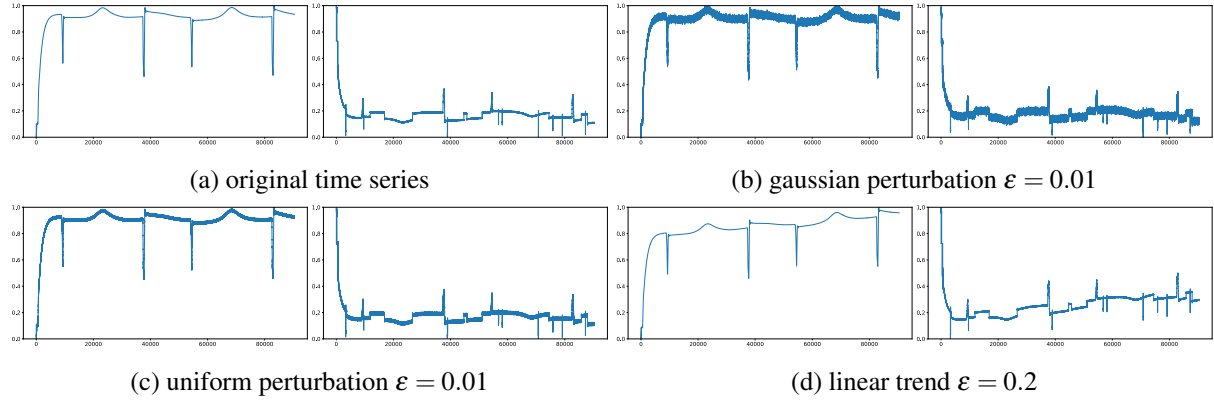


Figure 5: Example of time series and effect of some perturbations

- The linear trend transformation simulates a sensor degradation which makes a linear bias with derivative ε to be added to the series, causing the time series to slowly diverge, as can be seen in Fig 5d.
- The amplitude scaling transformation simulates a change of magnitude of percentage ε of the whole time series.
- The missing data perturbation simulates a loss of data due to communication problems, for example, and corresponds to randomly removing a percentage ε of data points.

2.3 Methodology

Formally verifying the local robustness of the whole classification algorithm for a given time series s and perturbation t at strength ε , as stated above, would boil down to formally computing the set $DP(P_\varepsilon^t(s))$ and then verifying via Marabou that $NN(DP(P_\varepsilon^t(s))) \subseteq Class(s)$. Unfortunately, this end-to-end formal verification process is not directly applicable to this classification algorithm. The formal computation of the set $DP(P_\varepsilon^t(s))$ is not tractable by the tools we know: the data processing phase is developed in Python, a language for which no formal analysis tool exists, and consists of complex mathematical computations that are hardly eligible for formal reasoning. Furthermore, in order to use the tool Marabou, we need to express the property to verify with interval constraints on the data points of the input.

Therefore, we decided to approximate the computation of the set $DP(P_\varepsilon^t(s))$ in the following way. For a given time series s , we apply the chosen perturbation to s a given number of times, to obtain a finite set of perturbed time series $S \subseteq P_\varepsilon^t(s)$. Then we compute $DP(S)$, the result of the data processing phase on this set of inputs to obtain their relevant anomaly C or D histograms. Finally, we determine an envelope around these histograms that intuitively should represent the set of all histograms that we could obtain by applying this perturbation at this strength on s . We denote by $u, v \in \mathbb{R}^M$ the minimum and maximum vectors around the histograms of $DP(S)$: $\forall h \in DP(S), \forall k \in \llbracket 1, M \rrbracket, u_k \leq h_k \leq v_k$. Then we denote by $Env_\varepsilon^t(s)$ the envelope containing all histograms between the two vectors u and v : $Env_\varepsilon^t(s) = \{h \in \mathbb{R}^M \mid u_k \leq h_k \leq v_k\}$. Note that this last set is neither an over- nor an under-approximation of the actual set $DP(P_\varepsilon^t(s))$, since we may miss some histograms that fall outside of this envelope, and we may also include histograms that cannot be resulting from a perturbation of the initial input. However, we experimentally established that this envelope is a rather good approximation.



Figure 6: Envelope around a C1 histogram with a Gaussian noise at 0.005

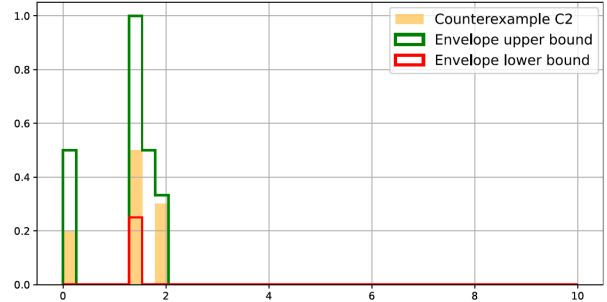


Figure 7: Counterexample found by Marabou in the envelope of Fig. 6

For example, we show on Figure 6 the result of the computation of this envelope on a time series initially classified as an anomaly C1, whose histogram h^C is shown in blue. We applied 10 times a Gaussian noise of strength $\epsilon = 0.005$ (meaning 0.5% of the amplitude of the signal) on this time series and obtained the envelope around their histograms determined by vectors u (in green) and v (in red).

To choose the number of perturbation iterations for envelope construction, we tested several values and observed the evolution of the envelope. Beyond 10 iterations, the envelope showed little change while runtime increased sharply. We therefore fixed the number at 10 as a good compromise between accuracy and efficiency.

For the perturbations that are generated with a randomness factor (Gaussian, Poisson and uniform noises, as well as missing data perturbation), perturbing the same time series 10 times produces different series, allowing us to create 10 distinct histograms, even though at low strengths, some histograms may be similar due to data processing. For other perturbations like linear trend, the perturbation is deterministic, so we explicitly vary the strength across a fixed range to generate different versions. For amplitude scaling, which is also deterministic, we similarly apply a sequence of increasing strengths (e.g., from 0.5ϵ to ϵ) to ensure we cover a range of effects and build a meaningful envelope.

Then we want to prove that all the histograms in this envelope are classified as the initial time series s . The tool Marabou answers queries in the form of formula (2) by transforming their negation into constraint satisfaction problems. It solves these problems by either giving an example that satisfies the problem (then a counterexample to the initial property) or proving that the problem is unsatisfiable (thus proving the initial property). Then it has to solve 3 different queries, one for each *target* class different from $Class(s)$:

$$\exists? h \in \mathbb{R}^M, h \in Env_\epsilon^t(s) \wedge NN(h) = target$$

If one of these queries is satisfiable, the histogram found is a counterexample to local robustness. Otherwise, we have proof that the neural network is locally robust to this perturbation at this strength, for s . Figure 7 shows in orange a histogram found by Marabou which is in the envelope computed around the C1 histogram of Figure 6 but is classified as a C2 anomaly, thus showing the non-robustness of the neural network around this histogram.

3 Evaluation Results for Local Robustness

We conducted our evaluation of local robustness only on correctly classified time series taken from series classified as anomaly C (urgency 1 to 3) and anomaly D (urgency 1 to 3), as well as two samples of series

classified as ‘no C’ and ‘no D’. The set of series classified as ‘no C’ is sampled from the set of all the time series that pass through the neural network responsible for classifying anomaly C but are not classified as an anomaly C (see Fig. 4). This includes all the time series that are classified as anomaly D (urgency 1 to 3), anomaly A urgency 1 and 2, and nominal. Likewise, the set of series classified as ‘no D’ by the other neural network are all the series classified as anomaly A urgency 1 and 2, and nominal. To maintain coherence with the distribution of the data, we sampled 300 series for each of these classifications. For ‘no C’, we sampled 50 entries from each of the 6 classes. For ‘no D’ we sampled 100 entries from each of the 3 classes.

To determine the relevant strengths to apply the chosen perturbations, we used the Signal-to-Noise Ratio (SNR) for each perturbation. For s a time series defined on n time units, p a perturbed version of this series defined on the same time frame:

$$\text{SNR}(s, p) = 10 \log_{10} \left(\frac{\text{Power}(s)}{\text{Power}(s - p)} \right) \quad \text{where } \text{Power}(s) = \frac{\sum_{k=1}^n s(i)^2}{n}$$

The SNR then quantifies the degradation of the signal: the higher the SNR, the more powerful is the actual signal, the lower the SNR, the more noise is present and the more information is lost. Figure 8 displays the SNR for each perturbation, except missing data whose SNR cannot be computed due to the missing values. As our goal is to identify the boundary at which local robustness is lost, and following domain experts knowledge, we tested perturbations with SNRs down to 20 dB for amplitude scaling and 35 dB for all other perturbations, under which the classifier always fails to remain robust.

Then we chose a sample of strength values from 0.001 up to the SNR threshold, on the logarithmic scale. The idea is to determine the maximal acceptable strengths required to keep the classification stable.

In Figure 9, we show the rate of time series for which the local robustness property is proven for each class and each strength of each perturbation. For a given class X , as in section 1.3, we denote by $N_c(X)$ the number of time series with status X correctly classified as X . For a perturbation t and a strength ε , we also denote by $N_{lr}(X, t, \varepsilon)$ the number of such time series for which the entire envelope $Env_\varepsilon^t(s)$ is also classified as X . We then define the local robustness rate as $N_{lr}(X, t, \varepsilon)/N_c(X)$. This indicator therefore measures the fraction of correctly classified time series of class X that remain robust under perturbation t of intensity ε .

- Figure 9a, 9b, and 9c: we can see that for similar SNRs, the two neural networks are much more robust to uniform noise than to other random noises, Poisson noise being the most challenging for classification.
- Figure 9d: linear trend perturbation for similar SNRs does not radically modify classification.
- Figure 9e: we applied the missing data perturbation with different percentages of missing data, from 0.1% to 50% and did not notice a radical change in classification for most of the classes.
- Figure 9f: we can see that the two neural networks are quite sensitive to amplitude scaling, more than a 2% scaling strongly affects classification.

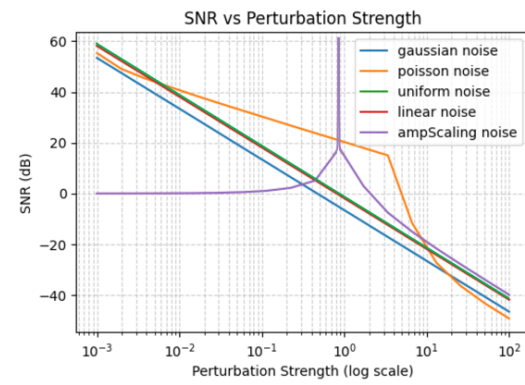


Figure 8: Signal-to-Noise Ratio for each perturbation

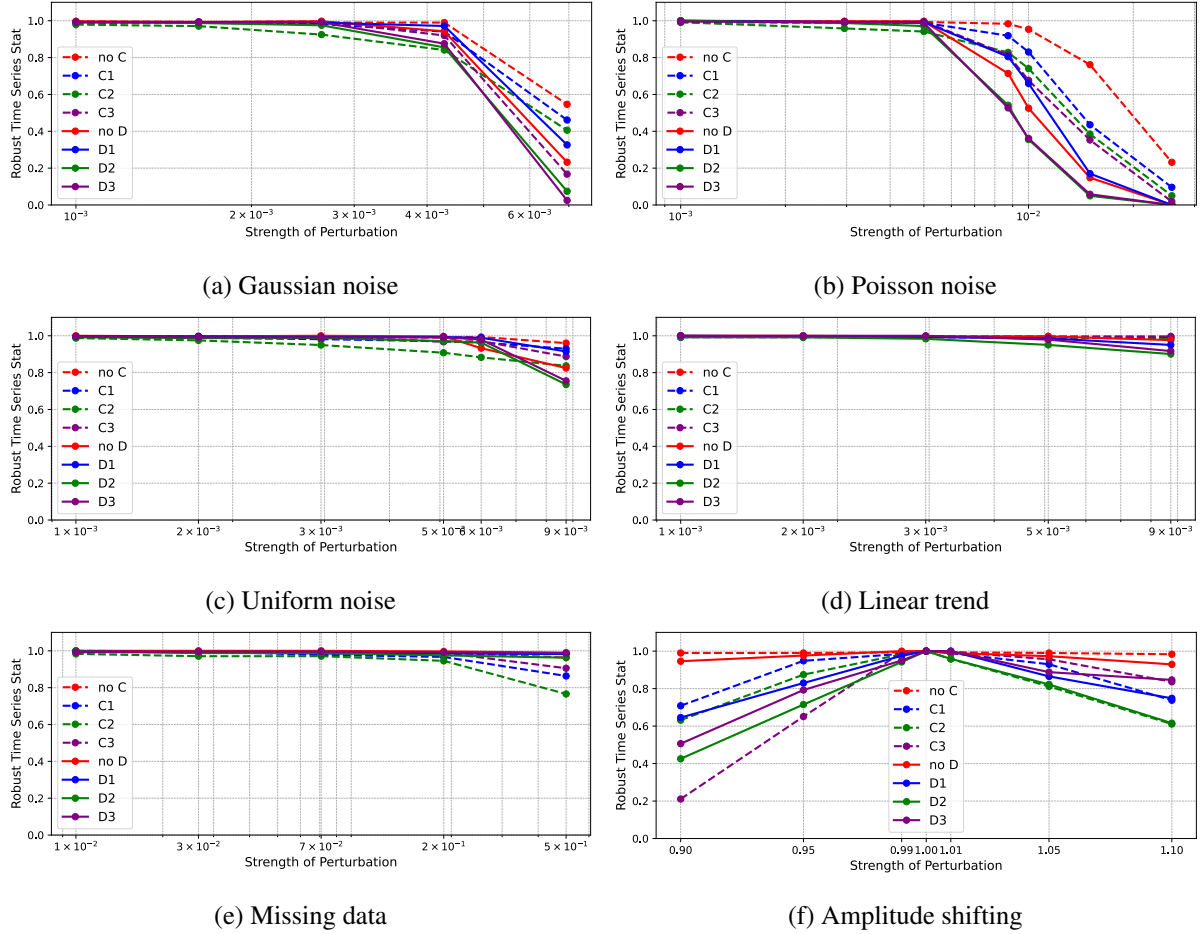


Figure 9: Local robustness of neural networks classifying anomaly C and D to the different perturbations, class by class

Since our neural networks are primarily designed to detect the presence of anomalies, local robustness is particularly important to ensure that the network does not fail to detect an anomaly (false negative) or incorrectly classifies a nominal instance as anomalous (false positive). This means that if, during the verification process for an anomaly of type C (regardless of urgency), we find a counterexample classified as a non-anomaly, then there is a risk that our model would fail to detect the anomaly under perturbation. In order to focus on the robustness of anomaly detection regardless of the anomaly urgency, we refined our previous robustness results by considering any misclassifications of an anomalous time series as nominal as a false positive.

In Figure 10, we visualize this property by distinguishing between the presence and absence of anomalies, as well as by the strength of each type of perturbation. Accordingly, we redefine $N_{lr}(X, t\epsilon)$ by interpreting X as a binary variable, distinguishing between C and ‘no C’, as well as D and ‘no D’. We notice that, when considering only anomaly detection, all the results are better than those displayed in Fig. 9, even if the general tendency remains the same for almost all perturbations.

- Figures 10a, 10b, and 10c: For similar SNRs, Gaussian and Poisson noise show a higher likelihood of the model missing anomalies, up to 100% for Poisson, under strong perturbations. In contrast,

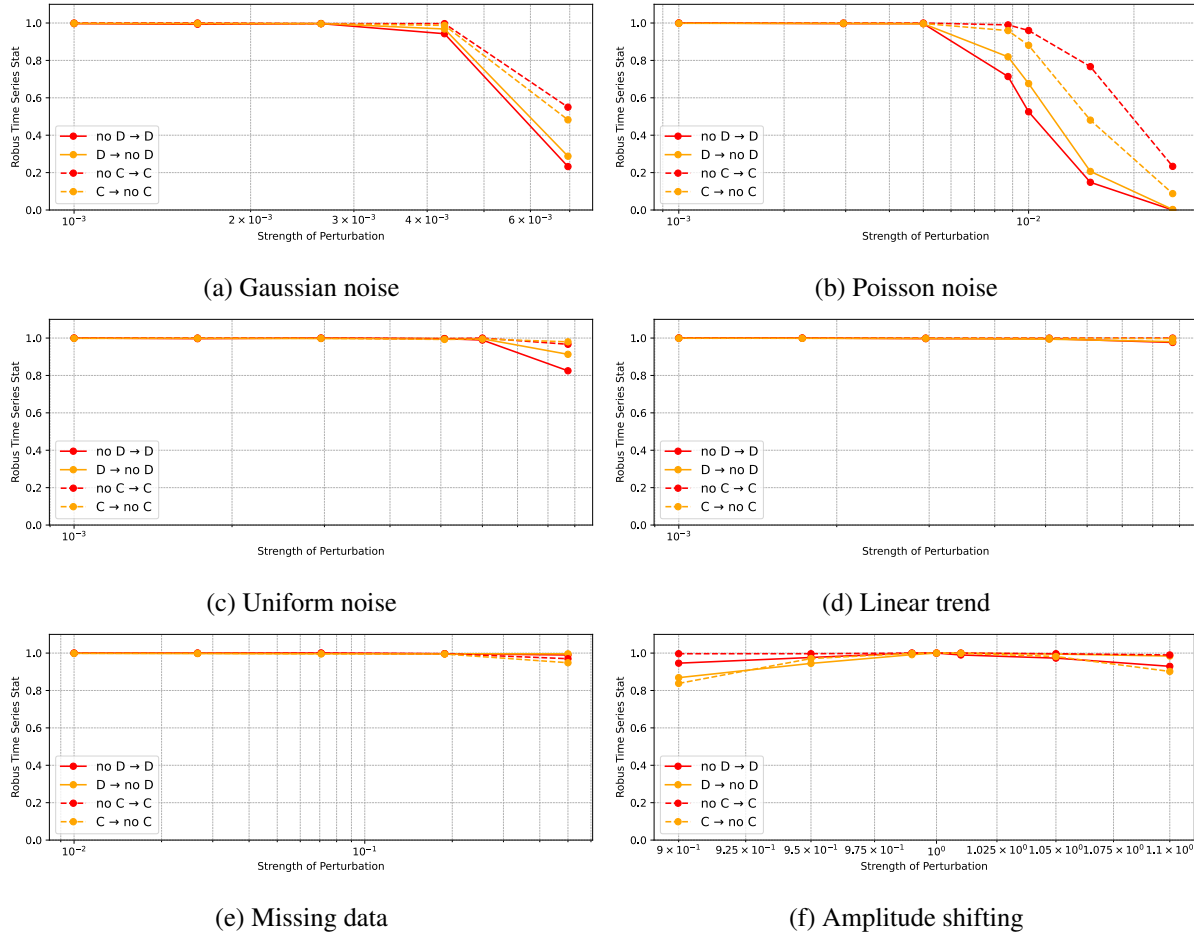


Figure 10: Local robustness of neural networks classifying anomaly C and D to the different perturbations, with respect to the detection of the anomaly

uniform noise appears more robust, as previously observed.

- Figures 10d and 10e: Linear trend perturbations and missing data perturbations result in relatively stable behavior across similar SNRs, indicating better robustness.
- Figure 10f: We observe that when changing the amplitude, the neural networks are more likely to misclassify an actual anomaly as a non-anomaly, rather than producing a false positive. While the neural networks seem to be very sensitive to this perturbation when considering class by class classification in Figure 9f, we can see here that they are quite robust when considering only the detection of anomalies regardless of the urgency.

4 Global Robustness

Besides local robustness, formal verification can be used more generally to help determine parts of the input domain where the classification algorithm is robust, therefore improving trustworthiness. Thus we worked on defining constraints for each anomaly histograms such that the classification is guaranteed. It

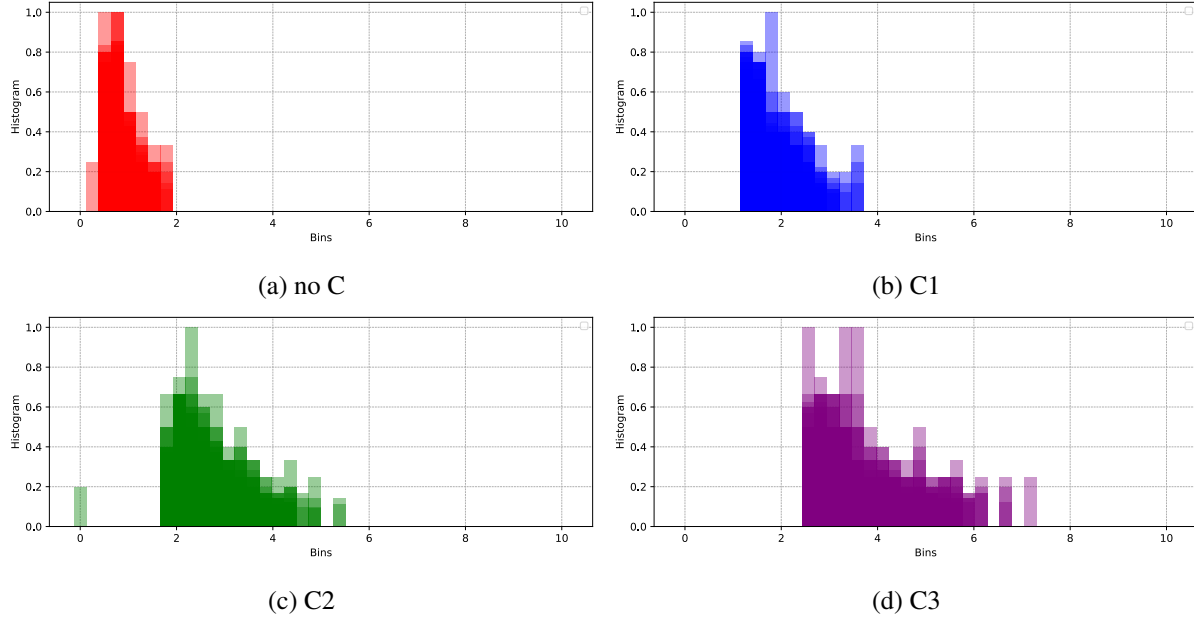


Figure 11: All histograms of anomaly type C

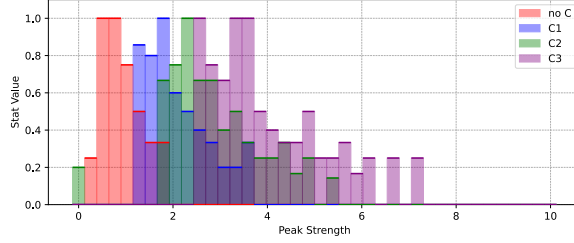


Figure 12: Upper bounds for classes of anomaly C

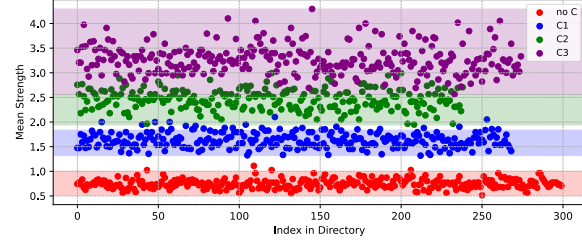


Figure 13: Weighted sums of all C histograms

means that for each class x , we want to define a finite set of constraints $(C_i^x)_{i=1}^L$ such that any histogram $h \in \mathbb{R}^M$ that satisfies all constraints $(C_i^x)_{i=1}^L$ is classified as x . Therefore, any time series or perturbed time series satisfying these constraints is guaranteed to be classified as x . Since we obtained results only for anomaly C, we restrict our analysis to this case.

To be as generic as possible, we want these constraints to be satisfied by a large majority of the histograms obtained from the training time series. That is the reason why, to define these constraints, we worked on generalizing some chosen characteristics of these histograms, like the minimum and maximum values possible at each point, the weighted sums, and local means when needed.

First, if we look at all the anomaly C histograms obtained from the correctly classified time series of the dataset, displayed in Figure 11, we can see that they have specific shapes and specific positions according to the class they belong to.

Based on these observations, we determined envelopes containing, for each class, all the histograms for that class. Figure 12 shows the upper bound at each point for each class of anomaly C, the lower bound always being 0. This first constraint alone is not sufficient to capture any particular class, because the intersections between envelopes are too large. Further analysis revealed that in certain cases, for

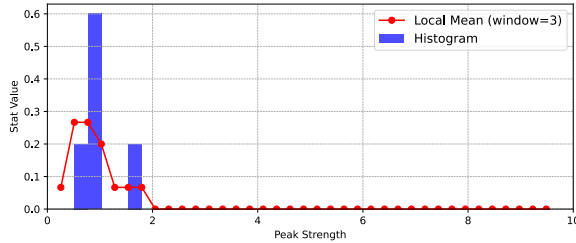


Figure 14: Sliding 3-sized window mean of a ‘no C’ histogram

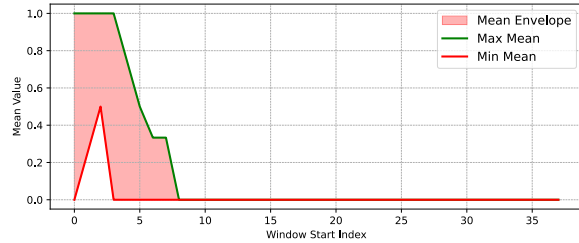


Figure 15: Minimum and maximum means for a sliding 3-sized window on all ‘no C’ histograms

anomaly C, the classes could be distinguished using the weighted sum of the histogram. The weighted sum of a histogram $h \in \mathbb{R}^M$ is the product of bin values with their indices: $\sum_{i=1}^M h_i \times i$. We analyzed the distribution of the weighted sums of all anomaly C histograms. Figure 13 shows that this feature does not clearly separate the different classes. However, we found that, when considered together with the envelopes defined above, well-chosen weighted sum intervals allow us to clearly discriminate between C1 and C3 anomalies, and also contribute to defining the ‘no C’ case. These intervals do not necessarily include all the histograms of a class obtained from the dataset, but they were determined so as to exclude as few histograms as possible. In practice, only 4 histograms for ‘no C’ (1.3%) and 30 histograms for C1 (11%) were excluded, while no histograms were excluded for C3.

For other classes, the weighted sum interval, even with the envelopes, is not sufficient, and a finer analysis at a local level had to be preferred. Specifically, for C2 and ‘no C’ classes, we computed mean values over sliding windows of fixed sizes across the histogram. For a given $k \in \llbracket 1, M \rrbracket$, the mean over the sliding window of size k is the vector $m \in \mathbb{R}^{M-k}$ defined by $\forall i \in \llbracket 1, M-k \rrbracket, m_i = \frac{1}{M} \sum_{j=i}^{i+M-1} h_j$. Figure 14 shows the sliding 3-sized window mean of a ‘no C’ histogram, and Figure 15 shows the results of minimum and maximum means for a sliding window of size 3 on all histograms of class ‘no C’.

Our experimentation shows that for class ‘no C’, windows of size 3 and size 4 provide the best separation from the other classes, together with the envelope and the weighted sum constraint. Unfortunately, for class C2 as well as for all classes of anomaly D, no set of constraints has yet been found that ensures a robust classification. To summarize, we formally proved the robustness of the neural network classifying anomaly C for the following cases.

Class	Constraints ensuring robustness
no C	‘no C’ envelope + Weighted sum in $[0.51, 1]$ + ‘no C’ envelope of 3-sized and 4-sized window means
C1	C1 envelope + Weighted sum in $[1.32, 1.83]$
C3	C3 envelope + Weighted sum $[2.56, 4.29]$

5 Conclusion

Our results demonstrate that using formal verification on a hybrid AI algorithm helps improve trustworthiness by providing guarantees essential to the deployment of critical fault detection systems in space applications. One of the main challenges in applying formal methods to industrial AI systems lies in the

data processing pipeline, which is often not amenable to formal reasoning. However, the design intuition behind these processes remains crucial in shaping a verification strategy. Our methodology enables a fine-grained analysis of the model’s behavior, identifying precisely where robustness breaks down and the system becomes unreliable, thus providing a practical measure of the model’s robustness limits.

The class by class counterexamples produced by our verification tool have value in various contexts: for instance, when a certain classification’s accuracy is critical, or when certain misclassifications can be tolerated. By grouping outputs into binary categories in our use case, we were able to draw meaningful local robustness conclusions, focusing on anomaly detection and not only on classification.

While the relevance of global robustness may be higher for functional specifications, our results suggest that this formal verification methodology can be extended to broader scenarios, helping define verified safe regions within the operational design domain (ODD).

Ultimately, our findings confirm that formal verification methods are mature enough to be applied in industrial contexts, even when the algorithms involving AI models are not fully designed with formal verification in mind.

References

- [1] Brian Armstrong-Helouvy (1991): *Control of machines with friction*. 128, Springer Science & Business Media.
- [2] Stanley Bak (2021): *nnenum: Verification of ReLU neural networks with optimized abstraction refinement*. In: *NASA Formal Methods Symposium*, Springer, p. 19–36.
- [3] Valdemir Carrara & Hélio Koiti Kuga (2013): *Estimating friction parameters in reaction wheels for attitude control*. *Mathematical Problems in Engineering* 2013(1), p. 249674.
- [4] Allan Y Lee & Eric K Wang (2015): *In-flight performance of Cassini reaction wheel bearing drag in 1997–2013*. *Journal of Spacecraft and Rockets* 52(2), pp. 470–480.
- [5] Augustin Lemesle, Julien Lehmann & Tristan Le Gall (2024): *Neural Network Verification with PyRAT*. arXiv preprint arXiv:2410.23903.
- [6] Mattia M Longato, Thomas Hughes, Vladimir Yotov & Guglielmo S Aglietti (2023): *Microvibration simulation of reaction wheel ball bearings*. *Journal of sound and vibration* 567, p. 117909.
- [7] Jonathan C. McDowell (2020): *General Catalog of Artificial Space Objects, Release 1.7.3*. Available at <https://planet4589.org/space/gcat>. Accessed: 2025-07-11.
- [8] Janusz Narkiewicz, Mateusz Sochacki & Bartłomiej Zakrzewski (2020): *Generic model of a satellite attitude control system*. *International Journal of Aerospace Engineering* 2020(1), p. 5352019.
- [9] Alejandro Penacho Riveiros, Yu Xing, Nicola Bastianello & Karl H. Johansson (2024): *Real-Time Anomaly Detection and Categorization for Satellite Reaction Wheels*. In: *2024 European Control Conference (ECC)*, IEEE, Stockholm, Sweden, p. 253–260, doi:10.23919/ECC64448.2024.10591184.
- [10] Alejandro Penacho Riveiros, Nicola Bastianello, Matthieu Barreau & Karl H. Johansson (2025): *Physics-Informed Detection of Friction Anomalies in Satellite Reaction Wheels*. In preparation.
- [11] Christopher J Seeton (2006): *Viscosity–temperature correlation for liquids*. *Tribology Letters* 22, pp. 67–78.
- [12] Zhouxing Shi, Qirui Jin, Zico Kolter, Suman Jana, Cho-Jui Hsieh & Huan Zhang (2025): *Neural Network Verification with Branch-and-Bound for General Nonlinearities*. In: *Tools and Algorithms for the Construction and Analysis of Systems, LNCS 15696*, Springer, pp. 315–335.
- [13] Haoze Wu, Omri Isac, Aleksandar Zeljić, Teruhiro Tagomori, Matthew Daggitt, Wen Kokke, Idan Refaeli, Guy Amir, Kyle Julian, Shahaf Bassan, Pei Huang, Ori Lahav, Min Wu, Min Zhang, Ekaterina Komenantskaya, Guy Katz & Clark Barrett (2024): *Marabou 2.0: A Versatile Formal Analyzer of Neural Networks*. In: *Computer Aided Verification, LNCS 14682*, Springer, pp. 249–264.